J. Fluid Mech. (2019), *vol.* 870, *pp.* 848–869.
doi:10.1017/jfm.2019.251

Particle transport induced by internal wave beam streaming in lateral boundary layers

E. Horne[1,4,†], F. Beckebanze[2,†], D. Micard[3,4], P. Odier[4], L. R. M. Maas[5] and S. Joubaud[4]

[1]LadHyX, CNRS, École Polytechnique, 91128 Palaiseau CEDEX, France

[2]Mathematical Institute, Utrecht University, P.O. Box 80010, 3508 TA Utrecht, The Netherlands

[3]LMFA UMR 5509 CNRS, Université de Lyon, École Centrale 69130 Écully Lyon, France

[4]Univ Lyon, ENS de Lyon, Univ Claude Bernard, CNRS, Laboratoire de Physique, F-69342 Lyon, France

[5]Institute for Marine and Atmospheric research Utrecht (IMAU), Utrecht University, Princetonplein 5, 3584 CC Utrecht, The Netherlands

(Received 5 October 2018; revised 18 March 2019; accepted 25 March 2019; first published online 15 May 2019)

Quantifying the physical mechanisms responsible for the transport of sediments, nutrients and pollutants in the abyssal sea is a long-standing problem, with internal waves regularly invoked as the relevant mechanism for particle advection near the sea bottom. This study focuses on internal-wave-induced particle transport in the vicinity of (almost) vertical walls. We report a series of laboratory experiments revealing that particles sinking slowly through a monochromatic internal wave beam experience significant horizontal advection. Extending the theoretical analysis by Beckebanze *et al.* (*J. Fluid Mech.*, vol. 841, 2018, pp. 614–635), we attribute the observed particle advection to a peculiar and previously unrecognized streaming mechanism in the stratified boundary layer originating at the lateral walls. This vertical boundary layer streaming mechanism is most efficient for significantly inclined wave beams, when vertical and horizontal velocity components are of comparable magnitude. We find good agreement between our theoretical prediction and experimental results.

Key words: boundary layer structure, internal waves, sediment transport

1. Introduction

Internal waves are ubiquitous in the global oceans, where they play a critical role in transporting sediments, nutrients and pollutants from localized sources to remote places (Alford 2003), with potentially strong influence on marine ecosystems (Woodson 2018). Many efforts have been undertaken to understand the behaviour of particles in the ocean. For the upper ocean, particle advection, dominated by ocean currents and surface waves, is reasonably well understood (van Sebille *et al.* 2018). In contrast, the mechanisms dominating suspended particle advection in the stratified

† Email addresses for correspondence: ernesto.horne@ladhyx.polytechnique.fr, f.beckebanze@uu.nl

interior and near the bottom of the abyssal ocean remain to be established clearly. In analogy to surface waves being important for particle advection near the surface, it is regularly invoked that internal waves must be relevant for particle advection near the sea bottom, both vertically through mixing related to breaking of waves and horizontally through induced (Lagrangian) transport. While internal-wave-induced sediment transport has been observed on continental shelves (Hosegood, Bonnin & van Haren 2004; Butman *et al.* 2006; Quaresma *et al.* 2007), field observations in the abyssal sea are largely hampered by the technical challenges.

Recent studies indicate that mixing in the vicinity of steep ocean topography is much stronger than previously thought (Mashayek *et al.* 2017; McDougall & Ferrari 2017), suggesting strong erosion of nearly neutrally buoyant particles into the water column right above the bottom. Coincidentally, internal wave motion is typically also enhanced above rough topography (Wunsch & Ferrari 2004; Garrett & Kunze 2007). This raises the question of how internal wave motion may facilitate advection of slowly sinking particles in the vicinity of steep topography. This study investigates boundary layer effects near steep topography on internal-wave-induced particle advection. Steep refers to the slope $\tan\alpha$ of the topography with respect to the horizontal being significantly larger than the slope $\tan\theta$ of the internal wave propagation.

We analyse a series of laboratory experiments (partially reported in chap. 5 in Horne (2015)) revealing that slowly sinking particles experience significant horizontal advection in the vicinity of an internal wave beam. Peculiarly, the observed particle advection is strongly dependent on the wave frequency ω_0 relative to the Brunt–Väisälä frequency, $N_0 = \sqrt{-(g/\langle\bar{\rho}\rangle)(\mathrm{d}\bar{\rho}/\mathrm{d}z)}$, where g is the acceleration of gravity, $\bar{\rho}(z)$ is the component of the density that monotonically increases with depth and is stationary, $\langle\bar{\rho}\rangle$ is the vertical average of $\bar{\rho}(z)$; therefore, the full density profile can be written as $\rho_0 = \bar{\rho}(z) + \rho$, where ρ represents the density perturbations. The goal of this study is to understand and rigorously describe the dynamics that dominates the experiments. We provide strong evidence that the observed particle displacement is facilitated by an internal-wave-induced horizontal mean flow.

Our theoretical analysis, extending the work by Beckebanze *et al.* (2018) to weakly nonlinear internal waves, highlights a previously unrecognized lateral-wall streaming mechanism. Streaming refers to irreversible mean flow generation through nonlinear internal wave interactions, in analogy to acoustic streaming (Lighthill 1978). Typically, streaming results in strong horizontal mean flow generation if mean vertical vorticity is produced. Here, 'strong' refers to persistent, cumulative transfer of energy from the wave field into the mean flow. Strong mean flow generation is known to occur due to horizontal cross-beam variation (Bordes *et al.* 2012; Kataoka & Akylas 2015; Semin *et al.* 2016; Couston *et al.* 2018; Beckebanze, Raja & Maas 2019), with important modifications by planetary rotation (Grisouard & Bühler 2012; Fan, Kataoka & Akylas 2018), and upon reflection where incident and reflected beams interact (Thorpe 1997; Grisouard *et al.* 2013; Zhou & Diamessis 2015; Raja 2018). Renaud & Venaille (2019) recently also found strong mean flow generation in a flat bottom boundary layer.

Our detailed analysis demonstrates that the lateral-wall streaming is related to a peculiar difference in the lateral boundary layer thickness for vertical and horizontal velocity components, first noted by Vasiliev & Chashechkin (2003), and recently linked to intensified wave field damping by Beckebanze *et al.* (2018). The lateral-wall streaming is strongest for significantly inclined wave beams, when vertical and horizontal along-wall velocity components are of similar magnitude, in agreement

with the experimentally observed dependency on the wave frequency. Note that we refer to such angles as significantly inclined angles to contrast them with the ocean environment, where most dominant waves have low frequency, and thus low angles. We remark that the previously unknown lateral-wall streaming was only recognized due to the absence of known streaming mechanisms in the experimental set-up. As such, it is likely to have also occurred in other laboratory experiments on internal waves, among which are the experiments on internal wave attractors by Hazewinkel (2010) and Brouzet *et al.* (2017), and possibly also in Semin *et al.* (2016). Importantly, this streaming mechanism in the stratified boundary layer is absent in homogeneous fluids, and thus fundamentally different from the well-known homogeneous streaming mechanisms summarized in Riley (2001). In the ocean, the stratified streaming mechanism may be secondary to the homogeneous streaming mechanism because the most energetic part of the oceanic internal wave field is quasi-horizontal.

The structure of this paper is as follows. In § 2 we report the laboratory set-up, including a detailed description of a newly developed particle injector in § 2.1. The experimental results (§ 3) are the motivation for the theoretical derivation of the internal-wave-induced mean flow near the lateral walls, presented in § 4. The multiple-scale analysis may be skipped as the main theoretical results are summarized in § 5, where we compare them to the experimental results. Oceanic circumstances for which our results are potentially important, as well as possible extensions and limitations of our study, are discussed in § 6.

2. Experimental set-up

A rectangular tank of inner size $L \times W \times H = 156 \times 17 \times 42.5$ cm^3, corresponding respectively to coordinates x, y and z, is filled up to $\sim$37 cm with a linearly salt-stratified fluid by using the two-bucket method (Fortuin 1960; Oster & Yamamoto 1963). Vertical density profile measurements are performed with a conductivity probe. The fluid densities at $z = 33.6$ cm, where the particles enter the fluid, and bottom ($z = 0$) are $\rho_0 = 0.998$ g cm^{-3} and 1.039 ± 0.002 g cm^{-3}, respectively, corresponding to a buoyancy frequency $N_0 = 1.1 \pm 0.03$ rad s^{-1}. Internal plane waves are created by an internal wave generator based on the set-up developed by Gostiaux *et al.* (2007).

The wave generator consists of 50 plates stacked vertically. Each plate extends over the full width of the tank W and is 6.5 mm high. We use the upper 25 plates (from $z = 17.35$ cm to $z = 33.6$ cm) for the forcing in the present experiments. We install the plates such that the oscillating plates mimic a sinusoidal vertical profile, with upward phase propagation and vertical wavelength $L_z = 3.9$ cm composed by 6 plates, over the vertical extent of $4.17L_z = 16.25$ cm. Figure 1(*a*) shows a composite snapshot of the steady-state wave beam and the column of settling particles described in § 2.1, here at $x = 40$ cm. The colour map visualizes the horizontal density perturbation, $\partial_x \rho$, derived from synthetic schlieren, which can be converted to any wave beam field quantity.

Eleven experiments are performed for imposed wave frequency ω_0 in the range 0.125–0.785 rad s^{-1}, all for fixed wave maker amplitude $A_0 = 0.9$ cm. The generated internal wave beam with characteristic wavelength $L_0 = L_z \cos\theta$ propagates downwards and to the right at angles $\theta = \sin^{-1}[\omega_0/N_0] = 0.11$–$0.8$ rad with respect to the horizontal. Table 1 summarizes the parameter values and ranges explored in this work. The along-beam decay (figure 1*b*) is extracted from a time series of 175 s (frames at 4 Hz), starting 50 s after the onset of the wave maker, filtered at the forcing

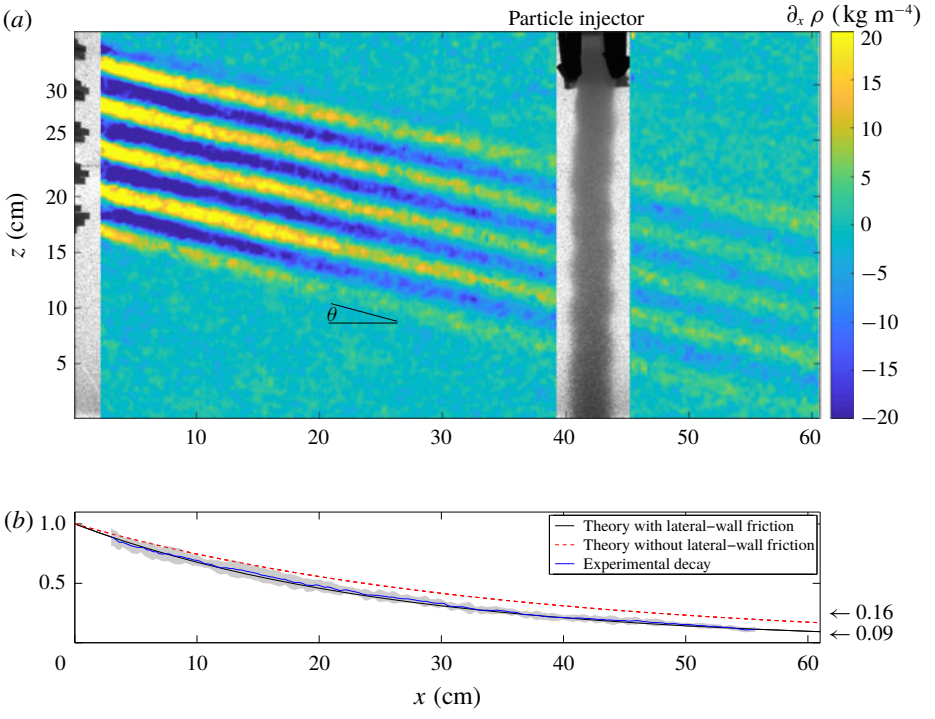

FIGURE 1. (Colour online) (*a*) Snapshot of the experimental internal wave beam, generated by the wave maker on the left ($x = 0$ cm) and extending over the full width of the tank (in the y direction), propagating downwards to the right with an angle $\theta = \sin^{-1}[\omega_0/N_0] = 15°$ with respect to the horizontal, and intersecting the sinking particle column, here at $x = 40$ cm from the wave maker. The colour map visualizes the horizontal density gradient, $\partial_x\rho$ (here, the vertical background density gradient is 72 kg m^4). (*b*) Spatially averaged along-beam decay of the wave field (normalized) extracted from ω_0-filtered time series (blue), with the grey shading indicating two standard deviations. The observation matches the theoretical exponential decay (derived in § 4) including both internal shear and lateral-wall friction (black line). Taking only internal shear dissipation into account (red dashed line) overpredicts the wave beam strength at $x = 60$ cm by approximately 80 % ($\approx 1 - 0.16/0.09$).

frequency $\omega_0 = 0.22$ rad s^{-1} for this case, and spatially averaging over 2 cross-beam wavelengths (300 data points). The exponential decay only matches the theoretical decay rate upon incorporating lateral-wall friction, emphasizing the importance of the lateral walls in the present experiments. The theoretical decay rates are derived in § 4. Viscous attenuation reduces the wave beam strength by ∼99.7 % at the end of the tank ($x = 156$ cm), making a sponge layer unnecessary. The wave field is observed using the synthetic schlieren technique, with a computer-controlled video camera (Allied Vision Technologies Stingray) with a CCD matrix of 2452 × 2054 pixels, which measures the variations of the gradient of density of the fluid (Sutherland *et al.* 1999; Dalziel, Hughes & Sutherland 2000). The conversion of pixels to distance varies by approximately 5 % throughout the tank, being 26 pix cm^{-1} at the back ($y = -W/2$) and 28.5 pix cm^{-1} at the front ($y = W/2$) of the tank. We apply the conversion

Parameter	Dimensional, in experiments	Non-dimensionalized
Wave frequency	$\omega_0 = 0.125$–0.785 rad s^{-1}	1
Along-beam velocity amplitude	$U_0 = A_0\omega_0 = 1$–7 mm s^{-1}	1
Cross-beam wavelength	$L_0 = \cos\theta L_z = 2.76$–$3.88$ cm	1
Vertical wavelength	$L_z = 3.9$ cm	$1/\cos\theta = 1.006$–1.435
Angle $\theta = \sin^{-1}[N_0/\omega_0]$	$\theta = 0.11$–0.79 rad	θ, same values
Brunt–Väisälä frequency	$N_0 = 1.1$ rad s^{-1}	$N = N_0/\omega_0 = 1/\sin\theta = 1.4$–$8.8$
Amplitude of wave maker forcing	$A_0 = 9$ mm	$U_0\cos\theta/(L_0\omega_0) = \epsilon\cos\theta = 0.23$
Width of the tank (in the y direction)	$W = 2l_yL_0 = 17.0$ cm	$2l_y = 4.4$–6.2
Height of wave maker and beam	$4.17L_z = 16.25$ cm	$2h = 4.17/\cos\theta = 4.2$–$5.9$
Boundary layer thickness	$d_0 = \sqrt{\nu/\omega_0} = 1.1$–$2.8$ mm	$\delta = d_0/L_0 = 0.04$–$0.08 \ll 1$
Decay rate due to internal shear	$\beta_1/L_0 = 0.02$–0.08 cm^{-1}	$\beta_1 = 0.07$–0.2
Decay rate due to wall friction	$\beta_2/L_0 = 0.005$–0.02 cm^{-1}	$\beta_2 = 0.02$–0.06
Stokes number at wave maker	$\epsilon = U_0/(\omega_0L_0) = 0.23$–$0.33$	ϵ, same value
Stokes number at particle column	$\epsilon_{18cm} = 0.05$–$0.15 \ll 1$	Same values

TABLE 1. Parameter values of the experiments and their corresponding non-dimensional values. Note that the Stokes number $\epsilon_x = \epsilon\exp[-(\beta_1 + \beta_2)x/L_0]$, quantifying the weak nonlinearity of the wave field, decreases strongly with distance to the wave maker. Both ϵ and δ are sufficiently small for our perturbation analysis to be valid.

26.8 pix cm^{-1} to the experimental data to match the experimentally determined wave beam height (in pixels) to the theoretically known wave beam height.

2.1. *Sinking particle column*

We developed a particle injector that allows for the production of a column of particles of controlled particle density, raining into the stratified fluid in a rectangular section, which embraces the full width of the tank (from wall to wall). The particle injector is placed at 18, 25 or 40 cm to the right of the wave generator. It is only at 18 cm that the particle column is located outside of the wave beam bottom reflection region for all tested wave frequencies, in which case we can rule out streaming effects associated with the interaction of incident and reflected beams. For this reason, we only analyse experimental particle column dynamics injected at an 18 cm distance from the wave maker.

The particles are injected between two vertical acrylic plates (see figure 1*a*) and slightly below the free surface through a slit in a copper tube, the slit extending along the entire y direction, from wall to wall. The distance between the acrylic plates (in along-wall x direction) is fixed at 3 cm for the present experiments. Beforehand, the particles are mixed with fresh water (density $\rho_0 = 0.998$ g cm^{-3}) and surfactant to avoid clustering during the immersion in the stratified fluid. The fresh water, acting as a carrier for the particles, drags the suspended particles from a small container

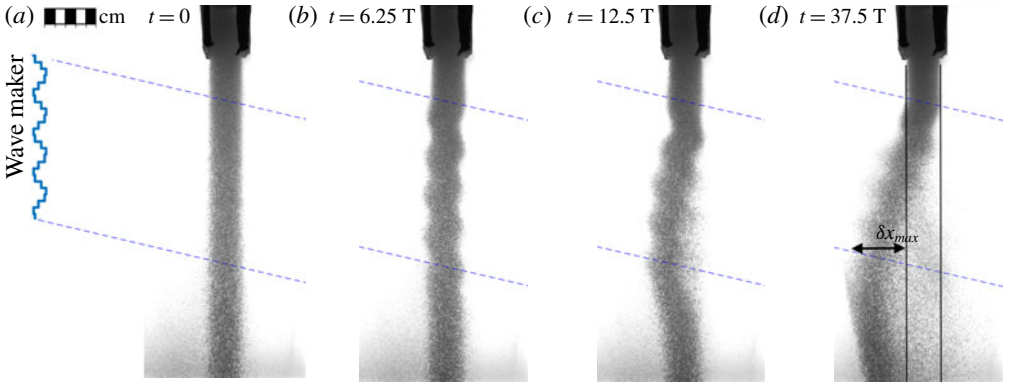

FIGURE 2. (Colour online) Snapshots at four instances (here, the wave period is $T = 20$ s) of the sinking particle column at 18 cm from the wave maker, intersected by the wave beam between the blue dashed lines. The wave maker is switched on at time $t = 0$ with a fully established column of sinking particles (panel *a*). The maximum horizontal displacement, δx_{max}, of the left edge of the sinking particle column is illustrated in panel (*d*).

(particle reservoir) through the copper tube to its slit transect. A peristaltic pump guarantees that the same amount of fluid is pumped into the slit transect of the copper tube as is sucked out of it. A constant flow rate of 20 ml min^{-1} for the carrier fluid results – after an initial transient phase – in a stationary homogeneous column with packing fraction $\phi \sim O(10^{-2})$. We verified experimentally that this small packing fraction does not affect the internal wave field.

The granular column consists of polystyrene grains with density $\rho_p = 1.055 \pm 0.01$ g cm^{-3}. (The particle density reported by the particle producer and in Horne (2015) is 1.05 g cm^{-3}, without any margin of error. Our own measurements – inferring particle densities from the height where particles come to rest in a linearly stratified fluid – revealed a slightly larger average particle density, with an estimated error of 0.01 g cm^{-3}.) The particle size of $O(100)$ μm was intended to be identical in all experiments. Indirect measurements of the prevailing particle sizes, derived from an experimental Doppler shift and explained in § A.4, indicate that the prevailing particle diameter increased in consecutive experiments, ranging from 40 to 240 μm. We believe that the carrier fluid segregated the particles, dragging smaller particles more efficiently, thereby first removing predominantly smaller particles from the particle reservoir. Only after comparison with our theoretical results – when repeating the experiments was no longer possible – did we realize that it would have been desirable to use higher-quality particles, with better-characterized particle sizes.

3. Experimental results

For each experiment, the wave maker is turned on once the column of settling particles is fully established in the quiescent stratified fluid (figure 2*a*), as described in § 2.1. The wave beam builds up quickly (over a few wave periods) and is in the steady state throughout most of the experiment, lasting 730 s (in some cases 750 s), corresponding to 15 to 90 wave periods, depending on the imposed wave frequency, ω_0. We observe that the internal wave beam perturbs the column, moving it back and forth with the wave beam motion, thus imprinting wiggles on the column

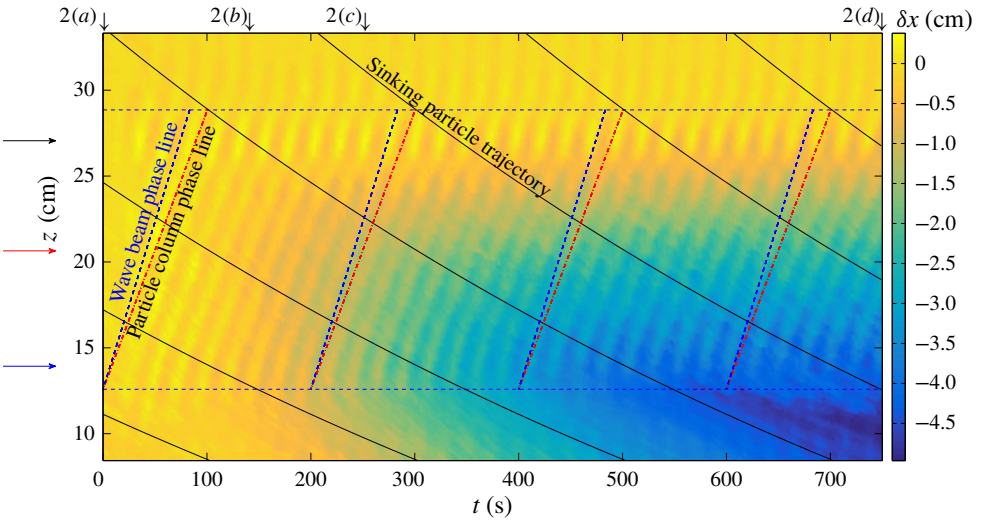

FIGURE 3. (Colour online) Displacement δx of the left edge of the sinking particle column (at 18 cm from the wave maker and for $\omega_0 = 0.31$ rad s^{-1}), as a function of height z (vertical) and time t (horizontal). Particles are subject to wave beam motion between the two blue dashed horizontal lines. The four black arrows at the top indicate the corresponding snapshots in figure 2; the three horizontal arrows at the left indicate the vertical levels at which time series are shown in figure 4(*a*). The column phase speed, $\omega_c/k_z = \omega_0/k_z + \bar{w}_p$, (indicated by four red dot-dashed lines, matching observed phase lines) differs from the wave beam phase speed, $\omega_0/k_z = 0.195$ cm s^{-1}, (four blue dashed lines) due to a Doppler shift. The average particle sinking velocity $\bar{w}_p$ is accurately determined from the difference between ω_0 and the experimentally estimated column oscillation frequency ω_c; see also figure 4(*b*). The curved downward-sloping lines show theoretical particle trajectories based on the average sinking velocity (here $\bar{w}_p \approx -0.03$ cm s^{-1} at $z = 20$ cm) determined from the Doppler shift, with the factor 2/3 slowdown from the surface towards the bottom due to a decreased density difference between the stratified fluid and the sinking particles (see § A.4).

snapshots in figures 1(*a*) and 2(*b–d*). In addition, throughout the experiment, the particle column is slowly shifted towards the wave maker (figure 2*b–d*), which is of particular interest because the driving mechanism behind this leftward particle column motion was initially unknown. We present the displacement of the left edge of the sinking particle column, δx, for the same experiment, as a function of height z and time t in a contour plot in figure 3, and at three vertical levels in figure 4(*a*). We find that the column displacement increases linearly from top to bottom of the wave beam interaction zone (figure 2*c–d*), suggesting that the settling particles are exposed to a depth-independent transport mechanism as they sink through the wave beam. In figure 2(*d*), the particles below the wave beam have been displaced horizontally before they fell out of the wave beam. This can also be deduced from figure 3, especially in the lower right corner of the plot.

Despite the overall movement to the left, we also observe that some particles are transported to the right (slightly visible in figure 2*d*). We interpret this transport to the right as a clear indication that the quasi-two-dimensional wave beam facilitates a particle transport that is non-uniform in the cross-tank direction (y), consistent with our theoretical explanation developed in § 4.

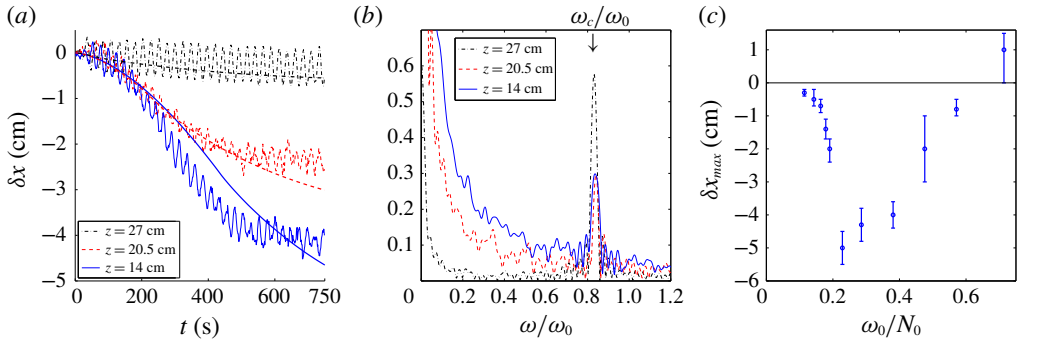

FIGURE 4. (Colour online) (*a*) Time series of the horizontal displacement δx of the left edge of the sinking particle column for the experiment with $\omega_0 = 0.31$ rad s^{-1} at three heights: near the top of the wave beam (black), half-way through (red) and near the lower edge of the wave beam (blue). The corresponding simulated mean column displacements (see § 4) are superimposed (smooth lines). (*b*) Corresponding spectra of experimental displacement time series, clearly peaking at the Doppler-shifted particle column frequency $\omega_c/\omega_0 = 0.84 \pm 0.02$, which gives an accurate sinking velocity estimate, $\bar{w}_p = 0.33 \pm 0.04$ mm s^{-1}. (*c*) Maximum horizontal displacement of the sinking particle column at the end of the experiments, for 11 different wave frequencies, all with $N_0 = 1.1$ rad s^{-1}.

We find that the strength of the horizontal column displacement, δx, is strongly dependent on the imposed wave frequency, ω_0. This is visualized in figure 4(*c*), where we present the maximum displacement of the left column edge, δx_{max}, for all eleven experiments. The maximum displacement, illustrated in figure 2(*d*), ranges from 0.3 to 5 cm to the left across the eleven experiments, with one exception for the experiment with the largest wave frequency ($\omega_0 = 0.785$), where we find a transport of $\sim$1 cm to the right. It is the peculiar horizontal displacement, the apparent non-uniformity in the cross-tank direction, and its strong dependence on the wave frequency, that we intend to explain by the theory developed in § 4.

4. Theory on mean flow generation at lateral walls

In this theoretical part we employ small-amplitude expansions to derive asymptotic expressions for monochromatic quasi-two-dimensional internal wave beams between two lateral walls, with viscous dissipation taken into account due to shear in the cross-beam direction and friction with the lateral walls. The exact solutions to the linearized equations, constructed in § 4.1, are used in § 4.2 to compute the induced mean field. In particular, we focus on the previously unrecognized mean vertical vorticity production in the stratified lateral-wall boundary layers, which drives a strong horizontal mean circulation.

4.1. *Internal wave beam between lateral walls*

For this theoretical analysis, we shall work with dimensionless variables (listed in table 1), employing $1/\omega_0$ as the time scale and the wavelength, L_0, as the length scale. The velocity is non-dimensionalized by $U_0 = A_0\omega_0$, which is the along-beam velocity amplitude based on an empirical parameterization by Mercier *et al.* (2010) for a vertically oriented, horizontally oscillating wave maker.

Denoting the dimensionless coordinates also by (x, y, z), we consider a linearly stratified Boussinesq fluid with scaled Brunt–Väisälä frequency $N = N_0/\omega_0 = 1/\sin\theta$ in an infinite domain between two lateral walls at $y = \pm l_y = W/2L_0$ and for $x \geqslant 0$.

The equations governing the dimensionless velocity field $\boldsymbol{u} = (u, v, w)$, buoyancy b, and pressure p of the Boussinesq fluid are given by

$$\partial_t \boldsymbol{u} + \epsilon(\boldsymbol{u}\cdot\boldsymbol{\nabla})\boldsymbol{u} = -\boldsymbol{\nabla} p + \delta^2 \Delta \boldsymbol{u} + \hat{\boldsymbol{z}} b, \quad \partial_t b + \epsilon\, \boldsymbol{u}\cdot\boldsymbol{\nabla} b = -N^2 w, \quad \boldsymbol{\nabla}\cdot\boldsymbol{u} = 0. \tag{4.1a–c}$$

Here, $\epsilon = U_0/(\omega_0 L_0) \ll 1$ is the Stokes number, and $\delta = d_0/L_0 \ll 1$ is the thickness of the Stokes boundary layer, $d_0 = \sqrt{\nu/\omega_0}$, scaled by wavelength L_0, and where $\nu = 1\ \mathrm{mm}^2\ \mathrm{s}^{-1}$ is the kinematic viscosity. We assume $\delta \ll l_y$ (that is, the dimensional half-width of the domain, $W/2 = l_y L_0$, is much larger than the Stokes boundary layer width, d_0). We solve (4.1) with no-slip boundary conditions, $\boldsymbol{u} = \boldsymbol{0}$ at $y = \pm l_y$ by expanding the velocity vector $\boldsymbol{u}$ in δ and ϵ,

$$\boldsymbol{u}(t) = \begin{pmatrix} u_0(t) \\ \delta v_1(t) \\ w_0(t) \end{pmatrix} + \begin{pmatrix} \bar{u}(\epsilon t) \\ \bar{v}(\epsilon t) \\ 0 \end{pmatrix} + \epsilon \begin{pmatrix} \bar{u}_1 \\ \bar{v}_1 \\ \bar{w}_1 \end{pmatrix} + O(\delta^2, \delta\epsilon, \epsilon^2), \tag{4.2}$$

and similarly for buoyancy b and pressure p, valid for the time range $t \in [0, O(\epsilon^{-1})]$. Additionally, we make the Ansatz that $\boldsymbol{u}^0 = [u_0, \delta v_1, w_0]$ oscillates at the imposed wave frequency, 1, (dimensionally ω_0). The overbar denotes the mean components, either varying only over the slow time, $\tau = \epsilon t$, or being constant, as is the case for the slaved mean flow, $\bar{\boldsymbol{u}}_1 = [\bar{u}_1, \bar{v}_1, \bar{w}_1]$. The slowly varying mean flow, $\bar{\boldsymbol{u}}(\epsilon t) = [\bar{u}, \bar{v}, 0]$, also referred to as vortical induced mean flow (Beckebanze *et al.* 2018) or strong mean flow (Bordes *et al.* 2012; Dauxois *et al.* 2018), is initially zero ($\bar{\boldsymbol{u}}(0) = \boldsymbol{0}$). Our objective is to understand how the leading-order wave field, $\boldsymbol{u}^0 = [u_0, \delta v_1, w_0]\mathrm{e}^{-\mathrm{i}t}$, forces the vortical induced mean flow at $O(\epsilon)$, possibly leading to $O(\epsilon^0)$-amplitudes for the vortical mean flow amplitudes, $\bar{\boldsymbol{u}}(\epsilon t)$ over $1/\epsilon$ time scales. We do not study wave–mean flow interactions (that is, possible feedbacks of the mean flow on the wave field).

Two-dimensional wave beam

Motivated by the experiments, we consider the internal wave energy propagation to be downwards along coordinate $\xi = x\cos\theta - z\sin\theta$, implying that the phase propagation is upwards along $\zeta = x\sin\theta + z\cos\theta$. The leading-order velocity field of transversally uniform wave beams solving (4.1) at $O(\delta^2, \epsilon^0)$-accuracy with free-slip conditions at the lateral walls can be expressed as

$$\boldsymbol{u}_0 = [u_0, v_0, w_0] = [\cos\theta, 0, -\sin\theta]U, \quad \text{with } U = \frac{1}{2\pi}\int_0^\infty \hat{U}(k)\mathrm{e}^{\mathrm{i}k\zeta - (\beta_1+\beta_2)(x/\cos\theta) - \mathrm{i}t}\,\mathrm{d}k. \tag{4.3}$$

Here, β_1 and β_2 are the viscous decay rates corresponding to internal shear dissipation and friction with the lateral walls, respectively. The physical quantities are always the real part of the presented expression. The spectrum $\hat{U}(k)$ of the along-beam velocity component is presumed to vanish for negative wavenumbers, $k < 0$, because the phase propagation is primarily along positive ζ. (It is known (Mercier *et al.* 2010; Beckebanze *et al.* 2019) that the upper and lower edges of the wave maker act as line sources, also radiating waves upwards. These upward-propagating waves, hardly visible in the experimental velocity field (figure 1*a*), are not relevant for the dynamics

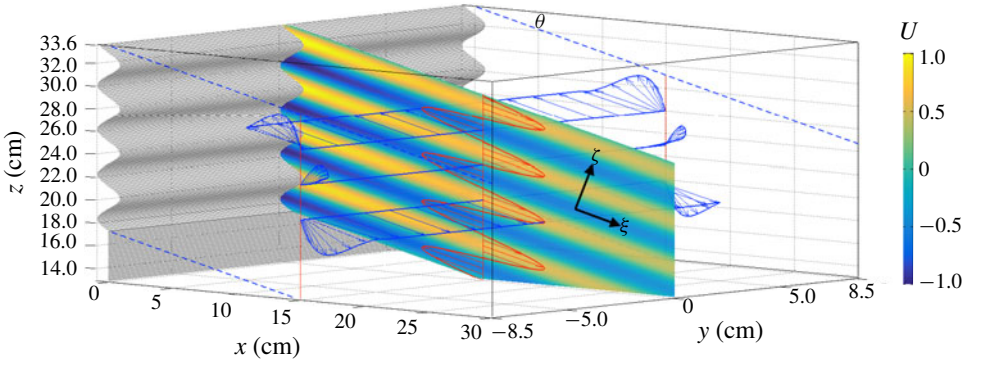

FIGURE 5. (Colour online) Snapshot of the theoretical along-beam velocity, U, in the centre plane, $y = 0$, with parameter values corresponding to the experiment with $\omega_0 = 0.31$ rad s^{-1}. The velocity vector $\boldsymbol{u}_0 = [u_0, 0, w_0]$ is presented at $x = 15$ cm along three cross-tank transects ($z = 19.9$, 22.95, 26 cm, blue arrows) and along a vertical transect in the centre plane (red arrows). For visualization purposes, the magnitude of the vector $\boldsymbol{u}_0$ is elongated by a factor 3 in the along-phase propagation direction, ζ. Note that near the lateral walls, the velocity vector $\boldsymbol{u}_0$ is not aligned with the along-beam direction, ξ. As a result, the in-product of $\boldsymbol{u}_0$ with ∇u_0 (pointing along the phase propagation direction, ζ) is non-negligible (see also figure 6*a*), causing strong mean flow generation near the lateral walls (shown in figure 7).

discussed here.) Replicating the laboratory experiment, we consider the along-beam velocity spectrum

$$\hat{U}(k) = \frac{\sin[h\cos\theta(k - 2\pi)]}{\pi(k - 2\pi)}, \tag{4.4}$$

generated by a wave maker of height $2h$ with vertical wavenumber $2\pi\cos\theta$ at $x = 0$, as depicted in figure 5.

The along-beam decay rate due to shear in the cross-beam direction ζ can be derived in various ways (see §6 in Voisin (2003) for an overview) and is given by $\beta_1 = \delta^2 \tan\theta k^3/2$. For the laboratory experiments with the cross-beam widths $2h\cos\theta = 4.17$, the spectrum $\hat{U}(k)$ peaks sharply at the imposed wavenumber 2π, justifying the use of the simplified internal shear decay rate $\beta_1 = 4\pi^3\delta^2\tan\theta$ for $k = 2\pi$. The decay rate β_2 obviously vanishes for free-slip conditions at the lateral walls, and is determined next upon imposing no-slip boundary conditions.

Lateral boundary layer

Following the analysis by Beckebanze & Maas (2016) and Beckebanze *et al.* (2018), we consider the momentum equations for u_0 and w_0 with subscript-derivative notation and in stretched transverse coordinate $\eta = \delta^{-1}y$:

$$-\mathrm{i}u_0 = -p_{0_x} + u_{0_{\eta\eta}}, \quad \mathrm{i}\cot^2\theta\ w_0 = -p_{0_z} + w_{0_{\eta\eta}}. \tag{4.5a,b}$$

Imposing no-slip boundary conditions at the walls, $\eta = \pm\delta^{-1}l_y$, and interior velocity field (4.3), gives

$$\left.\begin{aligned} u_0 &= \cos\theta(1 - E^x)U, \quad E^x(\eta) = \frac{\cosh[\mathrm{i}^{-1/2}\eta]}{\cosh[\mathrm{i}^{-1/2}\delta^{-1}l_y]}, \\ w_0 &= -\sin\theta(1 - E^z)U, \quad E^z(\eta) = \frac{\cosh[\mathrm{i}^{1/2}\cot\theta\eta]}{\cosh[\mathrm{i}^{1/2}\cot\theta\delta^{-1}l_y]}. \end{aligned}\right\} \tag{4.6}$$

The non-planar orbital structure of this along-beam velocity vector, $[u_0,\ w_0]$, is illustrated in figure 5. The velocity vector $\boldsymbol{u}_0 = [u_0,\ 0,\ w_0]$ has a non-zero divergence near the lateral walls due to the presence of stratification. Please note that for homogeneous lateral boundary layers, in which E^z and E^x are identical, the velocity vector $\boldsymbol{u}_0$ would be divergence-free. It is only due to the difference between E^x and E^z (caused by the stratification that modifies the vertical momentum equation in stretched coordinates, (4.5)) that we must include a $O(\delta)$-velocity term to satisfy the divergence-free constraint. Hence, by the continuity equation $u_{0_x} + w_{0_z} = -v_{1_\eta}$ at $O(\delta^0)$ in stretched coordinate (η), and using the impermeability boundary conditions $v_1 = 0$ at $y = \pm l_y$, we find the $O(\delta)$ transversal velocity

$$v_1 = \sin\theta \left(\mathrm{i}^{1/2} \cos\theta \frac{\sinh[\mathrm{i}^{-1/2}\delta^{-1}y]}{\cosh[\mathrm{i}^{-1/2}\delta^{-1}l_y]} - \mathrm{i}^{-1/2} \sin\theta \frac{\sinh[\mathrm{i}^{1/2}\cot\theta\delta^{-1}y]}{\cosh[\mathrm{i}^{1/2}\cot\theta\delta^{-1}l_y]} - \mathrm{i}^{1/2}\mathrm{e}^{\mathrm{i}\theta}\frac{y}{l_y} \right) U_\zeta. \tag{4.7}$$

The slow $O(l_y^{-1})$-decay of v_1 towards the interior, $-\mathrm{i}^{1/2}\sin\theta \mathrm{e}^{\mathrm{i}\theta} U_\zeta y/l_y$, requires an additional viscous attenuation factor, $\exp[-\beta_2\xi]$ with decay rate $\beta_2 = \delta l_y^{-1}\mathrm{Re}[\mathrm{i}^{-1/2}\sin\theta \mathrm{e}^{\mathrm{i}\theta}k]$, to satisfy the $O(\delta)$-continuity equation (Beckebanze & Maas 2016). Again, we may replace k by the dominant wavenumber, 2π. Despite the relatively thin boundary layers, we find that the friction with the lateral walls almost doubles the decay at 60 cm from the wave maker for the experiment depicted in figure 1.

4.2. *Induced Eulerian mean flow*

In this section, we construct the so-called induced mean flow, $\overline{\boldsymbol{u}} = [\bar{u}(\epsilon t) + \bar{u}_1,\ \bar{v}(\epsilon t) + \bar{v}_1,\ \bar{w}_1]$, generated through the time-averaged Reynolds stresses at $O(\epsilon)$. Balancing time-independent terms in the buoyancy equation at $O(\epsilon)$, one readily finds the vertical induced mean flow

$$\bar{w}_1 = -\frac{\epsilon}{N^2}\langle \mathrm{Re}[\boldsymbol{u}^0] \cdot \mathrm{Re}[\boldsymbol{\nabla} b_0] \rangle = -\frac{\epsilon}{2N^2}\mathrm{Re}[\boldsymbol{u}^0 \cdot \boldsymbol{\nabla} b_0^*] = \frac{\epsilon}{2}\mathrm{Im}[\boldsymbol{u}^0 \cdot \boldsymbol{\nabla} w_0^*], \tag{4.8}$$

where $\boldsymbol{u}^0 = [u_0,\ \delta v_1,\ w_0]$, $b_0 = -\mathrm{i}N^2 w_0$, and $\langle\cdot\rangle$ stands for time-averaging over one wave period, 2π. This weak (order-ϵ) induced mean vertical flow (in the Eulerian framework), also referred to as slaved mean flow, is exactly balanced by the vertical Stokes drift of the wave beam velocity field, $\boldsymbol{u}^0$, which we show in § A.2. Consequently, net mass transport can only take place in the horizontal plane, and we thus focus on the horizontal induced circulation.

Using a Helmholtz decomposition, the horizontal induced mean velocity field can be split into $[\bar{u},\ \bar{v}] = [\bar{\Psi}_y + \bar{\phi}_x,\ -\bar{\Psi}_x + \bar{\phi}_y]$, where $\bar{\Psi}$ and $\bar{\phi}$ are the stream function and flow potential, respectively. The flow potential describing the horizontal slaved mean flow, $[\bar{u}_1,\ \bar{v}_1] = [\bar{\phi}_x,\ \bar{\phi}_y]$, is set by the vertical slaved mean velocity, $\bar{w}_1$, through the continuity equation, $\bar{\phi}_{xx} + \bar{\phi}_{yy} = -\bar{w}_{1_z}$, and does not change over time for steady-state wave fields. Whereas the flow potential, $\bar{\phi}$, investigated by Kistovich & Chashechkin (2001), Tabaei & Akylas (2003) among others, may be relevant for truly two-dimensional wave fields (where $\bar{\phi}_y = 0$), it is typically secondary to the vortical flow described by the stream function, $\bar{\Psi}$, in the quasi-two-dimensional and three-dimensional configurations (Beckebanze *et al.* 2019). The mean vortical flow associated with $\bar{\Psi}$ can persistently accumulate energy until a strong large-scale circulation is established. The slow evolution equations of the potentially strong

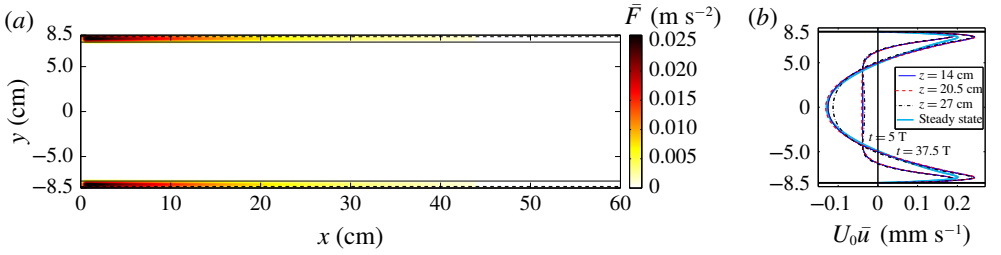

FIGURE 6. (Colour online) (*a*) Spatial structure of along-wall Reynolds stress, $\bar{F}$, expression (4.10), for parameter values corresponding to the experiment with $\omega_0 = 0.31$ rad s^{-1}, at $z = 20.5$ cm, vanishing almost everywhere except within a distance $(1 + \cot\theta)d_0 = 0.78$ cm of the lateral walls (indicated by solid lines). This distance is the sum of the homogeneous boundary layer thickness, $d_0 = \sqrt{\omega_0/\nu} = 0.18$ cm, (dashed lines) and the (stratified) boundary layer thickness of the vertical velocity component, $d_0 \cot\theta = 0.69$ cm. (*b*) Simulated mean flow in the x direction, $U_0\bar{u}$, along a cross-tank transect (y) at three vertical levels and $x = 17$ cm, at times $t = 5T$ and $t = 37.5T$. The thick light blue line corresponds to the theoretical steady-state mean velocity, derived in § 4.3.

horizontal vortical induced mean flow associated with stream function $\bar{\Psi}$, and no-slip boundary conditions at the tank boundaries, $x = 0, l_x$ and $y = \pm l_y$, are given by

$$\left.\begin{array}{c} \Delta_h \partial_\tau \bar{\Psi} = \epsilon^{-1}\delta^2 \Delta_h^2 \bar{\Psi} + \bar{F}_y \quad \text{with } \bar{F} = -\langle \mathrm{Re}[\boldsymbol{u}^0] \cdot \mathrm{Re}[\boldsymbol{\nabla} u_0] \rangle, \\ \bar{\Psi}(x, \pm l_y) = \bar{\Psi}_y(x, \pm l_y) = 0, \quad \bar{\Psi}(0, y) = \bar{\Psi}_x(0, y) = \bar{\Psi}(l_x, y) = \bar{\Psi}_x(l_x, y) = 0. \end{array}\right\} \tag{4.9}$$

Here, Δ_h is the horizontal Laplace operator, and $\tau = \epsilon t$ is the slow time over which the time-averaged $O(\epsilon)$-Reynolds stress divergence, $\epsilon\bar{F}$, acts as a $O(1)$-source of mean vertical vorticity. We also decoupled the three-dimensional induced mean flow problem into independent two-dimensional planar problems by neglecting shear in the vertical direction. This is an appropriate simplification, because lateral-wall friction turns out to dominate induced mean flow damping.

A lengthy but straightforward small-amplitude expansion (see § A.1) simplifies the mean Reynolds stress divergence, $\bar{F}$, to

$$\left.\begin{array}{c} \bar{F} = -\dfrac{1}{2}\mathrm{Re}[\boldsymbol{u}^0 \cdot \boldsymbol{\nabla} u_0^*] = \dfrac{\sin\theta \cos^2\theta}{2} \displaystyle\sum_{n=1}^{5} \mathrm{Im}\left[a_n \frac{\cosh[c_n \delta^{-1} y]}{\cosh[c_n \delta^{-1} l_y]}\right] \mathrm{Im}[U U_\zeta^*] + O(\delta l_y^{-1}, \delta^2) \\ \text{with } a_1 = -1 - \dfrac{\mathrm{i} e^{-\mathrm{i}\theta}}{\cos\theta}, \quad a_2 = 1, \quad a_3 = \tan\theta, \quad a_4 = -1, \quad a_5 = 1 + \mathrm{i}, \\ c_1 = \mathrm{i}^{-1/2}, \quad c_2 = \mathrm{i}^{1/2}\cot\theta, \quad c_3 = \mathrm{i}^{-1/2}(\cot\theta + 1), \\ c_4 = \mathrm{i}^{1/2}(\cot\theta + 1), \quad c_5 = \sqrt{2}. \end{array}\right\} \tag{4.10}$$

Here, we have absorbed the effects due to along-beam viscous dissipation in $O(\delta l_y^{-1}, \delta^2)$. The spatial structure of the mean Reynolds stress divergence, $\bar{F}$, which is practically zero everywhere except in a neighbourhood of $\delta(1 + \cot\theta)$ near the lateral walls (dimensionally $d_0(1 + \cot\theta)$), is presented in figure 6(*a*). Importantly, the magnitude of this $O(\delta^0)$-Reynolds stress divergence is independent of viscosity; it is the width $\delta(1 + \cot\theta)$ of the non-zero forcing regions of (4.10) that vanishes in the inviscid limit ($\delta \to 0$).

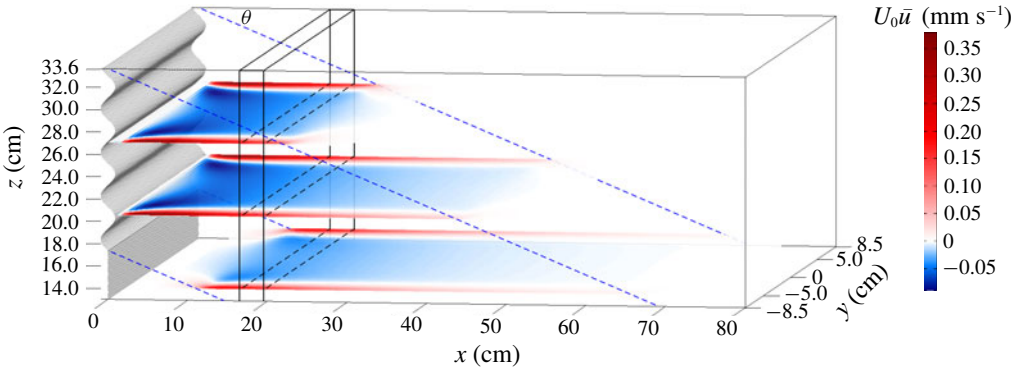

FIGURE 7. (Colour online) Visualization of the along-wall induced velocity, $U_0\bar{u}$, (in mm s^{-1}) at time $5T = 100$ s, in three horizontal planes ($z = 14$, 20.5 and 27 cm). The rectangular region where particles sink, centred at $x = 180$ mm, is sketched by the black box, and the wave beam motion is confined to the region between the blue dashed lines. Note that velocities in the boundary layer are a magnitude larger compared to the interior flow, and that the bottom of the plot ($z = 13$ cm) does not correspond to the bottom of the tank ($z = 0$).

Scaling analysis also reveals that the forcing due to transversal advection, $\langle \mathrm{Re}[\boldsymbol{u}^0] \cdot \mathrm{Re}[\nabla v_1] \rangle$, is at most $O(\epsilon\delta)$, hence it does not contribute to the leading-order Reynolds stresses at $O(\epsilon)$. Note also that in the interior, the largest Reynolds stresses are $O(\epsilon\delta l_y^{-1})$ due to viscous dissipation by the lateral walls, and $O(\epsilon\delta^2)$ due to internal shear dissipation. We solve (4.9) numerically on a rectangular grid, as explained in § A.3. Snapshots of the simulated induced mean flow in three horizontal planes are shown in figure 7, with three corresponding cross-tank transects in figure 6(*b*). Simulated induced mean velocities and associated particle column displacements for different wave frequencies are presented in figure 8.

4.3. *Steady-state-induced mean flow*

The objective is to derive a simple expression for the horizontal induced mean velocity. We simplify the problem by assuming the domain to be infinitely long in the along-tank x direction. Spatial variance of the Reynolds stress divergence $\bar{F}$ in the cross-tank y direction is much stronger than the decay in the along-tank x direction, $\exp[-2(\beta_1 + \beta_2)x/\cos\theta]$, which is the square of the wave beam decay due to viscous dissipation. Hence, we may assume that $\bar{F}$ varies predominately in the cross-tank y direction. By (4.9), $\epsilon\bar{F}_y$ is balanced by $\delta^2\Delta_h^2\bar{\Psi}$, reducing to

$$\delta^2\bar{\Psi}_{yyyy} = -\epsilon\bar{F}_y \quad \Leftrightarrow \quad \delta^2\bar{u}_{yyy} = -\epsilon\bar{F}_y. \tag{4.11}$$

Direct integration, and incorporating the boundary condition $\bar{u} = 0$ at $y = \pm l_y$, symmetry around $y = 0$ and zero net mass transport, $\int_{-l_y}^{l_y} \bar{u}\,\mathrm{d}y = 0$, gives

$$\bar{u} = \epsilon\frac{\sin\theta\cos^2\theta}{4}\mathrm{Im}[UU_\zeta^*]\left(\sum_{n=1}^{5}\mathrm{Im}\left[\frac{a_n}{c_n^2}\left(1 - 3\frac{y^2}{l_y^2} + 2\frac{\cosh[c_n\delta^{-1}y]}{\cosh[c_n\delta^{-1}l_y]}\right)\right]\right). \tag{4.12}$$

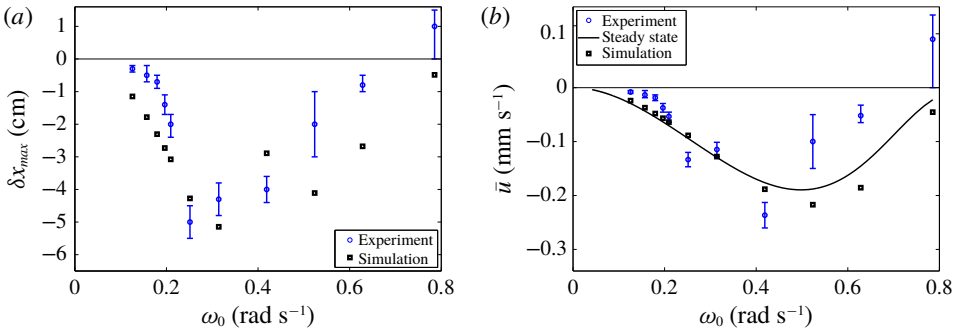

FIGURE 8. (Colour online) (*a*) Blue dots with error margins show the maximum observed displacement of the sinking particle column at the lower edge of the interaction zone with the wave beam. Black dots show the simulated column displacement, where we used the Doppler-shifted sinking velocity to determine how long particles take to sink through the wave beam with height 16.25 cm. (*b*) In the solid line, the theoretical steady-state-induced mean flow (see (4.13)) is compared with the simulated induced mean flow at $x = 165$ cm (black squares). The blue dots show the observed column displacement divided by its residence time in the wave beam interaction zone, with a maximum of 365 s.

We present this steady-state-induced mean velocity in figure 6(*b*) along a transect from wall to wall at $x = 18$ cm, and in figure 8(*b*) at the centre of the particle column, $(x, y) = (18, 0)$ cm, as a function of wave frequency ω_0. Note that some simulated mean velocities exceed the theoretical steady-state mean flow. This reveals that our assumption on the forcing $\bar{F}$ being uniform along the x direction slightly underestimates the simulated steady-state mean velocity. The theoretical time scale to reach the steady state is given by $W^2/(4\nu) \sim 2$ hours, though it appears to be already reached towards the end of the presented experiments.

Dimensionalizing expression (4.12), and approximating the sum by $(\sin\theta + 1)/(2\cos^2\theta)$, we find a characteristic value for the interior induced mean return flow:

$$U_0\bar{u}(y=0) \approx -\frac{\pi}{4}\sin\theta(1+\sin\theta)\frac{U_0^2}{L_0\omega_0}. \tag{4.13}$$

Interestingly, the magnitude of the steady-state-induced mean flow is independent of viscosity (ν) and of the distance between the lateral walls (W). This implies that the steady-state mean flow does not vanish in the limit of zero viscosity, whilst the driving Reynolds stress does vanish for zero viscosity. It is the time scale over which the steady state is reached that approaches infinity as viscosity vanishes or when the width of the domain goes to infinity.

The assumption that the y-variations of $\bar{F}$ are much stronger that the x-variations is appropriate if the along-wall forcing region (of size $2h\cot\theta$) is much larger than the wall-to-wall distance ($2l_y$). For relatively large wall-to-wall distances, $l_y \gg h\cot\theta$, two separate circulation cells are established in the vicinity of the walls.

In § 6 we consider oceanic conditions in which the interior return flow, equation (4.13), may be relevant.

5. Comparison between theoretical and experimental results

This section is devoted to a detailed comparison between the experimental results in § 3, and the theory derived in § 4, providing strong evidence that the observed particle

displacement is facilitated by the previously unrecognized internal wave lateral-wall streaming.

The theoretical results derived in detail in § 4 can be summarized as follows:

(i) The lateral walls modify the otherwise two-dimensional internal wave field. The most noticeable effect of the lateral walls on the linear internal wave beam dynamics is the additional viscous attenuation due to boundary friction, as discussed in § 3 and shown in figure 1(*b*).

(ii) Whereas in the interior the linear wave velocity vector is practically orthogonal to the phase direction, resulting in negligible nonlinear terms, this is not the case in the lateral boundary layers (figure 6*a*). The stratification causes differences in the boundary layer thickness for vertical and horizontal velocity components, producing strong nonlinearities near the lateral walls. The nonlinear Reynolds stresses, driving a mean flow, are strongest for strongly inclined beams, when vertical and horizontal velocity components are of similar magnitude. The strong dependency on the wave frequency ω_0 is a manifestation of the underlying dependency on the wave beam slope, $\tan\theta = \omega_0/\sqrt{N_0^2 - \omega_0^2}$.

(iii) The directly forced mean flow in the lateral boundary layers and in the direction of the horizontal beam propagation is balanced by a return flow through the interior. The return flow is initially nearly uniform in the interior if the stretch of along-wall forcing exceeds the wall-to-wall distance.

If the experimentally observed particle transport is facilitated by streaming at the lateral walls, then the observations should be consistent with the described theoretical results. We can compare temporal evolution, spatial patterns and ω_0-dependence of the particle displacement. In figure 4(*a*) we compare simulated and experimental evolution of the column edge at three vertical levels of the interaction zone of the sinking particle column and the wave beam. Whereas we find very good agreement at the top level, we attribute discrepancies at the middle and lower levels primarily to uncertainties in the residence time of particles within the interaction zone. Figure 7 illustrates that the directly forced flow at the lateral walls (in red) and the interior return flow (in blue) strongly decay with distance to the wave maker. Particles subject to the return flow are thus accelerated as they approach the wave maker – a feedback process that we did not take into account in the numerical simulations.

While the strength of the directly forced mean flow at the lateral walls varies strongly in the cross-tank direction, the return flow is initially roughly uniform in the cross-tank direction (see profile at $t = 5T$ in figure 6*b*). This is consistent with the observations: the sinking particle column is shifted to the left in the interior, maintaining a sharp left edge, while the particle advection to the right near the tank's boundaries blurs the right edge of the particle column (visible in the snapshots in figure 2*c*,*d*).

The strongest evidence for the lateral-wall streaming mechanism generating the observed horizontal particle displacement can be seen in the matching frequency dependency, presented in figure 8. Albeit large discrepancies at particular frequencies, it is the overall strong variation with ω_0 that matches surprisingly well. An exception is the experiment with the largest wave frequency ($\omega_0 = 0.785$ rad s^{-1}), which clearly shows transport towards the opposite direction, at odds with the boundary layer streaming hypothesis. It appears that the horizontal mean velocity field has changed sign, generating transport to the right, blurring the left column edge (not shown). It may be useful to remark that for this particular experiment, the beam slope, $\tan\theta = 0.87$, exceeded the maximum wave maker inclination, $L_z/(2\pi a_0) = 0.69$,

implying (theoretical) fluid motion through the wave maker plates, with possibly unknown nonlinear dynamics occurring at the wave maker.

Last but not least, we also find reasonable agreement between theoretical induced mean velocities and velocities inferred from the observed particle displacement (figure 8*b*).

6. Discussion and conclusions

Our study has revealed a previously unknown streaming mechanism by internal waves at the lateral walls. It was only due to the absence of known streaming mechanisms in this experimental set-up that the previously unrecognized streaming mechanism was discovered. As such, it seems plausible that the mechanism we describe also played a role in other internal wave experiments. The horizontal particle advection observed by Hazewinkel (2010) in the vicinity of an internal wave attractor (see figure 7.3 of the thesis) appears to be such a candidate, especially given the thin tank width of only 12 cm. Strong evidence of the lateral-wall streaming at play is also provided by the three-dimensional numerical simulations by Brouzet *et al.* (2016), where they found a lateral boundary layer intensified mean circulation in the vicinity of wave attractor branches (their figures 7 and 8). While it remains challenging to disentangle mean flow generation mechanisms in more complicated set-ups, we do believe that our lateral-wall streaming mechanism contributed to the induced mean flow observed both numerically and experimentally by King, Zhang & Swinney (2010) for tidal flow over three-dimensional topography.

Bordes *et al.* (2012) had also observed the generation of a mean flow in a stratified fluid, which was approximately an order of magnitude larger than what we observe. However, the mechanism was different, since it was based on transverse non-uniformity of the wave field, with a wave generator that did not span across the whole tank. This is not the case in our set-up, thus discarding this mechanism as a possible explanation for our observation of the mean flow.

It should be noted that the presented laboratory experiments were not designed to investigate the lateral-wall streaming mechanism and that the theoretical background was only provided when the experiment was not longer available. For future experiments we propose to include horizontal particle image velocimetry measurements, to get a more direct observation of the induced mean flow, especially near the lateral walls. Additionally, it was unclear until detailed comparison with our theory that the particle sizes varied strongly among the eleven experiments. This prevented us from using the traditional expression (A 7) to determine the sinking velocity. Instead, we derived the sinking velocity accurately from the Doppler-shifted column oscillation frequency, and subsequently used the expression (A 7) to infer the prevailing particle diameter, finding a factor of five difference among the eleven experiments. We believe that the large spread in particle size is caused by segregation of the carrier fluid in the newly designed particle injector. Changes in particle sizes among experiments may be prevented by using higher-quality particles with better-characterized particle sizes.

In the ocean, sites where internal waves propagate between two almost-vertical walls over distances longer than the channel width are sparse. A topographic feature similar to our laboratory set-up is the 500 m deep channel between two coral atolls studied by Rayson *et al.* (2018). As the length of the channel, roughly 10 km, exceeds the cross-channel width of 2–3, we may apply our simple expression (4.13) for the return flow. Using the observed M2 velocity amplitude of 0.2 m s^{-1}, a wavelength of 800 m (we

estimated a quarter wavelength from spatial variances in their figure 14), and Brunt–Väisälä frequencies ranging from 10^{-3} to 0.5×10^{-2}, we find a (theoretical) induced mean return flow of 1–5 cm s^{-1}. This is small compared to the observed, bottom-intensified mean current in excess of 1 m s^{-1} (Rayson *et al.* 2018). Nevertheless, it indicates that the streaming at the lateral walls can be relevant in the ocean. While it is legitimate to neglect the Coriolis effect at the coral atolls (taking it into account modifies the angle θ_{M2} by only 6 %), this may not be appropriate closer to the poles. Our analysis is not applicable to sites where the Coriolis frequency is similar to the strongest tidal component, typically M2. In spite of decreasing the slope $\tan^2\theta = (\omega_0^2 - f_0^2)/(N_0^2 - \omega_0^2)$ upon incorporating the Coriolis effect f_0 – thereby reducing the strength of the lateral-wall streaming – we do believe that the overall streaming is intensified in the presence of rotation due to the appearance of additional nonlinear terms associated with the rotational part of the wave field.

The directly forced mean flow in the vicinity of the boundary may be relevant for the transport of suspended sediment, nutrients and litter that is (occasionally) lifted into the near-bottom water column. Our theoretical analysis has revealed that mean flow generation is strongest for wave frequencies near the Brunt–Väisälä frequency (justifying the Coriolis effect to be neglected). Hence, we expect that small-scale internal wave packets associated with frequencies close to the local Brunt–Väisälä frequency (N_0) may facilitate along-boundary particle transport upon oblique reflections at steep topography, with 'oblique' meaning that the incident and reflected beams do not fall into the same vertical slice.

We speculate that there exists a continuous transition from our streaming mechanism at lateral (vertical) walls to the streaming mechanism over a flat bottom, recently investigated by Renaud & Venaille (2019). The viscous boundary layer description by Kistovich & Chashechkin (1995*a*,*b*) for supercritical internal waves reflecting at inclined boundaries may be a good starting point to extend the lateral-wall streaming analysis to oblique wave beam reflections at inclined boundaries. Furthermore, we propose to compute the boundary streaming upon oblique reflection at inclined walls for wave packets, both for well-studied spherical Gaussian shapes (Sutherland 2010) as well as elongated beam-like packets (Fan *et al.* 2018).

Acknowledgements

We thank three anonymous reviewers for their input leading to an improved manuscript. E.H. and F.B. are grateful to the organizers of the 2017 Les Houches summer school on Turbulent Flows in Climate Dynamics, where significant progress in writing this article was made. The collaboration was initiated at the FDSE summer school 2016 in Cambridge, UK, where D.M. introduced F.B. to the experimental results. F.B. is grateful for support by NWO Mathematics of Planet Earth grant 657.014.006. This work has been partially supported by the ONLITUR grant (ANR-2011-BS04-006-01) and partially achieved thanks to the resources of PSMN (Pôle Scientifique de Modélisation Numérique) of the ENS Lyon.

Appendix A

A.1. *Derivation of the Reynolds stress divergence expression, equation (4.10)*

We split $\bar{F} = -(1/2)\mathrm{Re}[\boldsymbol{u}^0 \cdot \nabla u_0^*] = -(1/2)\mathrm{Re}[u_0 u_{0_x}^* + w_0 u_{0_z}^*] - (1/2)\mathrm{Re}[v_1 u_{0_\eta}^*]$ into its along-wall components and wall-normal component, and derive their explicit

expressions separately. Using $U_x = \sin\theta U_\zeta + O(\delta l_y^{-1}, \delta^2)$ and $U_z = \cos\theta U_\zeta + O(\delta l_y^{-1}, \delta^2)$ allows us to write the time-averaged along-wall advection of u_0 at $O(\delta^0)$-accuracy as

$$\begin{aligned}-\frac{1}{2}\mathrm{Re}[u_0 u_{0_x}^* + w_0 u_{0_z}^*] &= -\frac{\cos^2\theta\sin\theta}{2}\mathrm{Re}[(-E^x + E^z + E^x E^{x^*} - E^z E^{x^*})UU_\eta^*] \\ &= \frac{\cos^2\theta\sin\theta}{2}\mathrm{Im}\left[-\frac{\cosh[c_1\delta^{-1}y]}{\cosh[c_1\delta^{-1}l_y]} + \frac{\cosh[c_2\delta^{-1}y]}{\cosh[c_2\delta^{-1}l_y]} + \frac{\cosh[c_5\delta^{-1}y]}{\cosh[c_5\delta^{-1}l_y]}\right. \\ &\quad \left. - \frac{\cosh[c_4\delta^{-1}y]}{\cosh[c_4\delta^{-1}l_y]}\right]\mathrm{Im}[UU_\zeta^*], \end{aligned} \tag{A 1}$$

because $\mathrm{Re}[UU_\zeta^*] = 0$, and constants c_n are defined in (4.10). Here, we have approximated $E^x E^{x^*}$ by $(\cosh[c_5\delta^{-1}y])/(\cosh[c_5\delta^{-1}l_y])$, which neglects a term of $\mathrm{e}^{-|O(\delta^{-1}l_y)|} \in O(\delta l_y^{-1})$, and similarly for $E^z E^{x^*}$. The along-wall advection thus sets the amplitudes $a_2 = 1$ and $a_4 = -1$ in (4.10), and contributes to $a_1 = -1 - \mathrm{i}\mathrm{e}^{-\mathrm{i}\theta}/\cos\theta$ and $a_5 = 1 + \mathrm{i}$. The remaining terms in the summation of (4.10) originate from the wall-normal advection term, $-(1/2)\mathrm{Re}[v_1 u_{0_\eta}^*]$. Writing the y-velocity component $v_1 = \sin\theta\cos\theta(-\mathrm{i}E_\eta^x + \mathrm{i}\tan^2\theta E_\eta^z - \mathrm{i}^{1/2}((\mathrm{e}^{\mathrm{i}\theta}\delta\eta)/(\cos\theta l_y)))U_\zeta$ in terms of E_η^x and E_η^z gives at $O(\delta^0)$-accuracy

$$\begin{aligned}-\frac{1}{2}\mathrm{Re}[v_1 u_{0_\eta}^*] &= -\frac{\sin\theta\cos\theta}{2}\mathrm{Re}\left[\left(-\mathrm{i}E_\eta^x + \mathrm{i}\tan^2\theta E_\eta^z - \mathrm{i}^{1/2}\frac{\mathrm{e}^{\mathrm{i}\theta}\delta\eta}{\cos\theta l_y}\right)U_\zeta \cdot \cos\theta E_\eta^{x^*} U^*\right] \\ &= \frac{\sin\theta\cos^2\theta}{2}\mathrm{Im}\left[-\mathrm{i}E_\eta^x E_\eta^{x^*} + \mathrm{i}\tan^2\theta E_\eta^z E_\eta^{x^*} - \mathrm{i}^{1/2}\frac{\mathrm{e}^{\mathrm{i}\theta}\delta\eta}{\cos\theta l_y}E_\eta^{x^*}\right]\mathrm{Im}[U^* U_\zeta] \\ &= \frac{\cos^2\theta\sin\theta}{2}\mathrm{Im}\left[\mathrm{i}\frac{\cosh[c_5\delta^{-1}y]}{\cosh[c_5\delta^{-1}l_y]} + \tan\theta\frac{\cosh[c_2\delta^{-1}y]}{\cosh[c_2\delta^{-1}l_y]}\right. \\ &\quad \left. - \frac{\mathrm{i}\mathrm{e}^{-\mathrm{i}\theta}}{\cos\theta}\frac{\cosh[c_1\delta^{-1}y]}{\cosh[c_1\delta^{-1}l_y]}\right]\mathrm{Im}[UU_\zeta^*]. \end{aligned} \tag{A 2}$$

Here, we approximated $(y/l_y)\sinh[c_1^*\delta^{-1}y]$ by $\cosh[c_1^*\delta^{-1}y]$, which again neglects a term of $\mathrm{e}^{-|O(\delta^{-1}l_y)|} \in O(\delta l_y^{-1})$. We also exploited the simple relation $\mathrm{Im}[U^* U_\zeta] = -\mathrm{Im}[UU_\zeta^*]$, and similarly for the term involving $E_\zeta^{x^*}$. Evidently, the wall-normal advection sets $a_2 = \tan\theta$, and contributes $+\mathrm{i}$ to a_5 and $-\mathrm{i}\mathrm{e}^{-\mathrm{i}\theta}/\cos\theta$ to a_1.

A.2. *Misconceptions concerning Stokes drift*

Horne (2015) suggested that the Stokes drift of the wave beam facilitated the observed particle transport, motivated by simple calculations adopted by Hazewinkel (2010). This appendix points towards subtle misconceptions that led both Hazewinkel (2010) and Horne (2015) to misleading interpretations of their experimental results.

By definition, the Stokes drift is the difference of the time-averaged Lagrangian and Eulerian flow (Longuet-Higgins 1953):

$$\boldsymbol{u}_S = \langle \boldsymbol{u}_L \rangle - \langle \boldsymbol{u} \rangle = \epsilon \left\langle \nabla \boldsymbol{u}(\boldsymbol{x}, t) \cdot \int_0^t \boldsymbol{u}(\boldsymbol{x}, t')\,\mathrm{d}t' \right\rangle + O(\epsilon^2), \tag{A 3}$$

with the time-averaging over one wave period, $\langle\cdot\rangle := 1/T\int_{t_0}^{t_0+T}\cdot\,\mathrm{d}t$, starting at arbitrary time t_0. Horne (2015) made the inappropriate choice $t_0 = 0$ in his analysis, which

corresponds to assuming all particles enter the wave beam at one particular point in time, rather than at any (random) point in time during one wave cycle. Repeating the analysis by Horne (2015), we find a particle column widening without net horizontal displacement upon averaging t_0 over $[0, T]$. Both Hazewinkel (2010) and Horne (2015) assumed $\langle \boldsymbol{u} \rangle = 0$, an assumption that is not true at $O(\epsilon)$, the leading order of the Stokes drift. It is well known (Wunsch 1971; Ou & Maas 1986; Zhou & Diamessis 2015; Beckebanze *et al.* 2019) and straightforward to determine from (A 3) that the vertical Stokes drift component is identical (with opposite sign) to the vertical induced mean velocity, $\langle w \rangle = \bar{w}_1$, given by (4.8), such that the Lagrangian mean flow in the vertical direction vanishes at its leading order:

$$\langle w_L \rangle = \langle w \rangle + w_S = 0 + O(\epsilon^2). \tag{A 4}$$

For two-dimensional fluids, mass conservation and the presence of vertical walls also require the horizontal Lagrangian mean flow component to vanish. This simple analysis stresses that horizontal cross-beam variations are necessary to generate net particle transport.

A.3. *Numerical simulations*

We solve (dimensionalized) (4.9) for the stream function $\bar{\Psi}_0^n$ at time $t = n\,\mathrm{d}t$ numerically on a rectangular domain, $(x, y) \in [0, 80] \times [-8.5, 8.5]$ cm^2, with 151 grid points in each direction, and time step $\mathrm{d}t = 1$ s. Employing standard central difference discretization in space and Euler backward (EB) in time we obtain:

$$(\tilde{L} - \mathrm{d}t\nu\tilde{B})\bar{\Psi}_0^{n+1} = \tilde{L}\bar{\Psi}_0^n + \mathrm{d}tU_0^2 k_0 \bar{F}_y. \tag{A 5}$$

Here, $\tilde{L}$ is the conventional 5-node discretized Laplace operator with Dirichlet boundary constraints, and $\tilde{B}$ is the conventional 13-node discretized biharmonic operator, using Dirichlet boundary constraints for first-neighbour nodes outside the domain and Neumann boundary constraints for second neighbours. While $\tilde{L}$ and $\tilde{B}$ are sparse, the related inverse, $\tilde{T} = (\tilde{L} - \mathrm{d}t\nu\tilde{B})^{-1}$, computed only once and used iteratively to solve (A 5) forward in time, is an almost full $m \times m$-matrix, with $m = 149^2$. Conveniently, most matrix elements of $\tilde{T}$ are negligibly small, and we can set matrix elements below a certain threshold (here 10^{-8}) to zero – retaining only 20 % non-zero matrix elements – without noticeable effects on the simulation.

Simulations with grid size 101×101 reveal increases of 1–10 % in simulated particle displacements after 730 s. This numerical error is acceptable, as it is of the same order as the approximations associated with the perturbation expansion and smaller than uncertainties of the experimental results. Simulations for the induced mean horizontal flow with free-slip boundaries predict particle displacements by a factor $\sim$10 larger, clearly indicating that the induced mean flow is damped primarily by lateral-wall friction.

A.4. *Particle trajectory and sinking velocity from Doppler shift*

In order to compare the experimental results (§ 3) on particle advection with the theoretical wave-induced mean flow (§ 4) we briefly discuss the relevant particle dynamics.

The time scale associated with adjustment to the motion of the fluid for neutrally buoyant spherical particles is $2a^2/9\nu$ (Maxey & Riley 1983), where a is the particle radius. For our experiments, the adjustment time for the suspended particles is of the order of a few milliseconds. As such, the particle motion, $\boldsymbol{u}_p$, can be described as a superposition of the mean particle sinking velocity, $\bar{w}_p$, and the motion of a fluid parcel at the particle's position, $\boldsymbol{x}_p(t) = [x_p(t), y_p(t), z_p(t)]$:

$$\boldsymbol{u}_p = \boldsymbol{u}(\boldsymbol{x}_p(t), t) + \hat{\boldsymbol{z}}\bar{w}_p(z_p(t)). \tag{A 6}$$

The Stokes particle sinking velocity is given by

$$\bar{w}_p(z) = \frac{2a^2 g}{9\nu}(1 - zN_0^2/g - \rho_p/\rho_0) < 0, \tag{A 7}$$

where $\rho_p = 1.055 \pm 0.01$ g cm^{-3} is the particle density, which is larger than the fluid density at the bottom of the tank, $\rho_0 = 1.039 \pm 0.002$ g cm^{-3}.

As mentioned in § 2.1, the particle radius a varies strongly among the eleven experiments, making (A 7) useless to determine the sinking velocity. Instead, we make use of a Doppler shift to determine the particle sinking velocity, as explained in the following. We can approximate the trajectory of a particle passing z at time t', by $z_p(t) = (t - t')\bar{w}_p$. Inserting this linearized particle trajectory into the leading-order wave beam field quantity (for example, $u_0(x, y, z, t) \propto \exp[\mathrm{i}(k_x x + k_z z - \omega_0 t)]$), we find that the velocity of the sinking particle column edge is given by $u_c(x, y, z, t) \propto \exp[\mathrm{i}(k_x + k_z(z - z_p(t)) - \omega_0 t)]$, which oscillates at the Doppler-shifted frequency $\omega_c = k_z\bar{w}_p + \omega_0$. We can accurately extract the Doppler-shifted column frequencies from the time series (see figure 4*a*,*b*), allowing us to determine the mean sinking velocity

$$\bar{w}_p = \frac{\omega_c - \omega_0}{k_z} < 0. \tag{A 8}$$

without knowledge of the particle sizes. Subsequently, we can determine the particle size from the sinking velocity, using (A 7). For our experiments, we found that the particle diameter ranged from 40 to 240 μm, with an increase of particle size in consecutive experiments. The value of 200 μm, reported by Horne (2015), falls into this range, but is clearly not representative for all experiments. As mentioned above, we believe that the large spread in particle sizes is caused by segregation of the carrier fluid that transports the particles from the particle reservoir to the particle injector.

Note that due to the stratification, the density difference, $\bar{\rho}(z) - \rho_p$, reduces by approximately a factor 2/3 from top to bottom in the laboratory experiments with $N_0 = 1.1 \pm 0.03$ rad s^{-1}, fresh water (with density 0.998 g cm^{-3}) at the surface and particle density $\rho_p = 1.055 \pm 0.01$ g cm^{-3}. For the linear stratification, it is straightforward to solve $\dot{z}_p^S(t) = \bar{w}_p^S = \bar{w}^S(z_p^S(t))$ for the associated particle trajectories starting at the particle injector, $z = h$, at time $t = t_0$:

$$z_p(t) = h(-0.5 + 1.5\exp[-2(t - t_0)\bar{w}_p(h)/(3h)]). \tag{A 9}$$

This particle trajectory is superimposed on the space–time particle column displacement diagrams (figure 3).

REFERENCES

ALFORD, M. H. 2003 Redistribution of energy available for ocean mixing by long-range propagation of internal waves. *Nature* **423**, 159–162.

BECKEBANZE, F., BROUZET, C., SIBGATULLIN, I. N. & MAAS, L. R. M. 2018 Damping quasi-two-dimensional internal wave attractors by rigid-wall friction. *J. Fluid Mech.* **841**, 614–635.

BECKEBANZE, F. & MAAS, L. R. M. 2016 Damping of 3d internal wave attractors by lateral walls. In *Proceedings of the VIIIth International Symp. on Stratified Flows*, pp. 1–6. University of California at San Diego.

BECKEBANZE, F., RAJA, K. J. & MAAS, L. R. M. 2019 Mean flow generation by three-dimensional non-linear internal wave beams. *J. Fluid Mech.* **864**, 603–626.

BORDES, G., VENAILLE, A., JOUBAUD, S., ODIER, P. & DAUXOIS, T. 2012 Experimental observation of a strong mean flow induced by internal gravity waves. *Phys. Fluids* **24** (4), 086602.

BROUZET, C., ERMANYUK, E., JOUBAUD, S., PILLET, G. & DAUXOIS, T. 2017 Internal wave attractors: different scenarios of instability. *J. Fluid Mech.* **811**, 544–568.

BROUZET, C., SIBGATULLIN, I. N., SCOLAN, H., ERMANYUK, E. V. & DAUXOIS, T. 2016 Internal wave attractors examined using laboratory experiments and 3D numerical simulations. *J. Fluid Mech.* **793**, 109–131.

BUTMAN, B., ALEXANDER, P. S., SCOTTI, A., BEARDSLEY, R. C. & ANDERSON, S. P. 2006 Large internal waves in Massachusetts Bay transport sediments offshore. *Cont. Shelf Res.* **26** (17–18), 2029–2049.

COUSTON, L.-A., LECOANET, D., FAVIER, B. & LE BARS, M. 2018 Order out of chaos: slowly reversing mean flows emerge from turbulently generated internal waves. *Phys. Rev. Lett.* **120** (24), 244505.

DALZIEL, S. B., HUGHES, G. O. & SUTHERLAND, B. R. 2000 Whole-field density measurements by 'synthetic schlieren'. *Exp. Fluids* **28** (4), 322–335.

DAUXOIS, T., JOUBAUD, S., ODIER, P. & VENAILLE, A. 2018 Instabilities of internal gravity wave beams. *Annu. Rev. Fluid Mech.* **50**, 1–28.

FAN, B., KATAOKA, T. & AKYLAS, T. R. 2018 On the interaction of an internal wavepacket with its induced mean flow and the role of streaming. *J. Fluid Mech.* **838**, R1.

FORTUIN, J. M. H. 1960 Theory and application of two supplementary methods of constructing density gradient columns. *J. Polym. Sci.* **44** (144), 505–515.

GARRETT, C. & KUNZE, E. 2007 Internal tide generation in deep ocean. *Annu. Rev. Fluid Mech.* **39**, 57–87.

GOSTIAUX, L., DIDELLE, H., MERCIER, S. & DAUXOIS, T. 2007 A novel internal waves generator. *Exp. Fluids* **42** (1), 123–130.

GRISOUARD, N. & BÜHLER, O. 2012 Forcing of oceanic mean flows by dissipating internal tides. *J. Fluid Mech.* **708**, 250–278.

GRISOUARD, N., LECLAIR, M., GOSTIAUX, L. & STAQUET, C. 2013 Large scale energy transfer from an internal gravity wave reflecting on a simple slope. *Procedia IUTAM* **8**, 119–128.

HAZEWINKEL, J. 2010 Attractors in stratified fluids. PhD thesis, Utrecht University, The Netherlands.

HORNE, E. 2015 Transport properties of internal gravity waves. PhD thesis, Université de Lyon, France.

HOSEGOOD, P., BONNIN, J. & VAN HAREN, H. 2004 Solibore-induced sediment resuspension in the Faeroe–Shetland Channel. *Geophys. Res. Lett.* **31**, 1–4.

KATAOKA, T. & AKYLAS, T. R. 2015 One three-dimensional internal gravity wave beams and induced large-scale mean flows. *J. Fluid Mech.* **769**, 621–634.

KING, B., ZHANG, H. P. & SWINNEY, H. L. 2010 Tidal flow over three-dimensional topography generates out-of-forcing-plane harmonics. *Geophys. Res. Lett.* **37**, L14606 1–5.

KISTOVICH, Y. V. & CHASHECHKIN, Y. D. 1995*a* Reflection of packets of internal waves from a rigid plane in a viscous fluid. *Atmos. Ocean. Phys.* **30**, 718–724.

KISTOVICH, Y. V. & CHASHECHKIN, Y. D. 1995*b* The reflection of beams of internal gravity waves at a flat rigid surface. *Z. Angew. Math. Mech.* **59**, 579–585.

KISTOVICH, Y. V. & CHASHECHKIN, Y. D. 2001 Mass transport and the force of a beam of two-dimensional periodic internal waves. *Z. Angew. Math. Mech.* **65**, 237–242.

LIGHTHILL, J. 1978 Acoustic streaming. *J. Sound Vib.* **61**, 391–418.

LONGUET-HIGGINS, M. S. 1953 Mass transport in water waves. *Phil. Trans. R. Soc. Lond.* A **245** (903), 535–581.

MASHAYEK, A., FERRARI, R., MERRIFIELD, S., LEDWELL, J. R., ST LAURENT, L. & NAVEIRA GARABATO, A. 2017 Topographic enhancement of vertical turbulent mixing in the Southern Ocean. *Nature Commun.* **8**, 14197.

MAXEY, M. R. & RILEY, J. J. 1983 Equation of motion for a small rigid sphere in a nonuniform flow. *Phys. Fluids* **26** (4), 883–889.

MCDOUGALL, T. J. & FERRARI, R. 2017 Abyssal upwelling and downwelling driven by near-boundary mixing. *J. Phys. Oceanogr.* **47** (2), 261–283.

MERCIER, M. J., MARTINAND, D., MATHUR, M., GOSTIAUX, L., PEACOCK, T. & DAUXOIS, T. 2010 New wave generation. *J. Fluid Mech.* **657**, 308–334.

OSTER, G. & YAMAMOTO, M. 1963 Density gradient techniques. *Chem. Rev.* **63** (3), 257–268.

OU, H. W. & MAAS, L. R. M. 1986 Tidal-induced buoyancy flux and mean transverse circulation. *Cont. Shelf Res.* **5** (6), 611–628.

QUARESMA, L., VITORINO, J., OLIVEIRA, A. & DA SILVA, J. C. B. 2007 Evidence of sediment resuspension by nonlinear internal waves on the western Portuguese mid-shelf. *Mar. Ecology* **246** (2–4), 123–143.

RAJA, K. J. 2018 Internal waves and mean flow in the presence of topography. PhD thesis, University Grenoble Alpes, France.

RAYSON, M. D., IVEY, G. N., JONES, N. L. & FRINGER, O. B. 2018 Resolving high-frequency internal waves generated at an isolated coral atoll using an unstructured grid ocean model. *Ocean Model.* **122**, 67–84.

RENAUD, A. & VENAILLE, A. 2019 Boundary streaming by internal waves. *J. Fluid Mech.* **858**, 71–90.

RILEY, N. 2001 Steady streaming. *Annu. Rev. Fluid Mech.* **33**, 43–65.

VAN SEBILLE, E., GRIFFIES, S. M., ABERNATHEY, R., ADAMS, T. P., BERLOFF, P., BIASTOCH, A., BLANKE, B., CHASSIGNET, E. P., CHENG, Y., COTTER, C. J. *et al.* 2018 Lagrangian ocean analysis: fundamentals and practices. *Ocean Model.* **121**, 49–75.

SEMIN, B., FACCHINI, G., PÉTRÉLIS, F. & FAUVE, S. 2016 Generation of a mean flow by an internal wave. *Phys. Fluids* **28** (9), 096601.

SUTHERLAND, B. R. 2010 *Internal Gravity Waves*. Cambridge University Press.

SUTHERLAND, B. R., DALZIEL, S. B., HUGHES, G. O. & LINDEN, P. F. 1999 Visualization and measurement of internal waves by 'synthetic schlieren'. Part 1. Vertically oscillating cylinder. *J. Fluid Mech.* **390**, 93–126.

TABAEI, A. & AKYLAS, T. R. 2003 Nonlinear internal gravity wave beams. *J. Fluid Mech.* **482**, 141–161.

THORPE, S. A. 1997 On the interactions of internal waves reflecting from slopes. *J. Phys. Oceanogr.* **27** (9), 2072–2078.

VASILIEV, A. Y. & CHASHECHKIN, Y. D. 2003 Generation of 3D periodic internal wave beams. *Z. Angew. Math. Mech.* **67**, 397–405.

VOISIN, B. 2003 Limit states of internal wave beams. *J. Fluid Mech.* **496**, 243–293.

WOODSON, C. B. 2018 The fate and impact of internal waves in nearshore ecosystems. *Annu. Rev. Mar. Sci.* **10** (1), 421–441.

WUNSCH, C. 1971 Note on some Reynolds stress effects of internal waves on slopes. *Deep-Sea Res.* **18**, 583–591.

WUNSCH, C. & FERRARI, R. 2004 Vertical mixing, energy, and the general circulation of the oceans. *Annu. Rev. Fluid Mech.* **36**, 281–314.

ZHOU, Q. & DIAMESSIS, P. J. 2015 Lagrangian flows within reflecting internal waves at a horizontal free-slip surface. *Phys. Fluids* **27** (12), 126601.